ADVANCED OPTICAL MATERIALS
www.advopticalmat.de

Fully Transparent Ultraviolet Photodetector with Ultrahigh Responsivity Enhanced by MXene-Induced Photogating Effect

Hailong Ma, Huajing Fang, Yanyu Liu, Jiaqi Li, Kai Jing, Jiawang Hong,* and Hong Wang**

Transparent photodetectors with the optical signal recognition and conversion capabilities are the core component for smart sensors and next-generation "see-through" optoelectronics. However, it is usually difficult to have both excellent optical transmittance and photoresponse performance, which hinders the practicality of transparent photodetectors. Herein, a photogating effect enhanced transparent ultraviolet (UV) photodetector is demonstrated based on the TiO_2/MXene van der Waals heterojunction. By simply spin-coating MXene nanosheets on TiO_2 film, the UV photodetector exhibits significantly enhanced performance, such as ultrahigh responsivity (202.4 A/W), large specific detectivity (1.79×10^{14} Jones) and outstanding external quantum efficiency (1.02×10^5%), which are three orders of magnitude higher than those of pure TiO_2 film. Meanwhile, the device exhibits up to 95% transparency in the visible range. Both the experimental results and theory calculations indicate that local Schottky junctions are established at the TiO_2/MXene interface. These local junctions exert a giant photogating effect under illumination, which can facilitate the separation of photogenerated carriers and improve the photodetection performance. Moreover, the transparent photodetector has been successfully applied in a UV index wireless sensing system. This work demonstrates the ingenious application of MXene in optoelectronics and provides insight into the design of high-performance transparent photodetectors.

1. Introduction

As one of the most important optoelectronic components, photodetectors that can convert optical signals into electrical signals have wide applications in many fields such as military, medical, environmental monitoring, and machine vision.[1–4] With the boom of transparent electronics in recent years,[5–9] transparent photodetectors have drawn increasing interest because the extra "see-through" feature will adapt them to special occasions and broadens their application area where traditional opaque photodetectors may not be applicable. For example, Zhang et al. developed a novel 3D camera based on transparent graphene photodetector stacks, which can simultaneously capture images on multiple focal planes and then build a complete 3D scene through an algorithm.[10] Brongersma and co-workers have proposed a conceptual design of transparent multispectral photodetector based on Si nanowire arrays, opening up a promising platform of transparent optical interfaces between a viewer and the outside world.[11] Our group has demonstrated a self-powered transparent photodetector with ultrafast response speed which plays the role of a "see-through" optical signal receiver in ultraviolet (UV) communication system.[9] For transparent photodetectors, both high responsivity and transmittance are required, which poses great challenges to the material selection and structure design of the device. In order to maintain a satisfactory transmittance (>70%), devices are often fabricated at the expense of photoresponse

H. Ma, H. Fang, J. Li, K. Jing
State Key Laboratory for Mechanical Behavior of Materials
School of Material Science and Engineering
Xi'an Jiaotong University
Xi'an 710049, China
E-mail: fanghj@xjtu.edu.cn

Y. Liu, J. Hong
School of Aerospace Engineering
Beijing Institute of Technology
Beijing 100081, China
E-mail: hongjw@bit.edu.cn

Y. Liu
College of Physics and Materials Science
Tianjin Normal University
Tianjin 300387, China

H. Wang
Department of Materials Science and Engineering
Southern University of Science and Technology
Shenzhen 518055, China
E-mail: wangh6@sustech.edu.cn

The ORCID identification number(s) for the author(s) of this article can be found under https://doi.org/10.1002/adom.202300393

DOI: 10.1002/adom.202300393

performance. Therefore, new materials and strategies need to be studied urgently to realize transparent photodetectors with high responsivity.

The responsivity of photodetectors is fundamentally determined by the dynamics of photogenerated carriers. During a typical photodetection process, electron-hole (e-h) pairs are first generated in semiconductors under illumination, then they are separated, transported, and collected driven by an external bias or a built-in electric field.[12,13] Therefore, facilitating the separation of photogenerated e-h pairs so that they can be collected before recombination is the key to improving the responsivity. A common approach is to apply a gate voltage that traps specific types of carriers at the interface between the gate dielectric and the photoactive layer, thereby suppressing the recombination of photogenerated e-h pairs.[14–16] However, the extra applied gate voltage not only complicates the detection system, but also easily leads to leakage current and increased energy consumption. Although some other studies employ ferroelectric polarization field or photovoltage as "gate voltage",[17–20] they still suffer from complicated device fabrication process and poor compatibility with transparent electronics. In contrast, the photogating effect is regarded as a facile method to improve responsivity by trapping certain types of carriers through defects or artificially designed hybrid structures.[21–23] Current researches on the photogating effect mainly focus on low-dimensional materials with photoresponse in the visible to infrared range and most cases exhibit limited responsivity enhancement depending on the band alignment.[24–28] So far, transparent photodetectors based on the photogating effect have not been reported, especially in the UV band. It remains a big challenge to effectively improve the responsivity of transparent photodetectors through photogating effect without affecting its spectral response.

To solve this problem, we turned our attention to an emerging class of two-dimensional (2D) materials. MXenes, namely transition metal carbides, and nitrides represented by $Ti_3C_2T_x$ (T stands for the surface terminations such as -O, -OH, and -F), provide new options for high-performance electronic and optoelectronic devices due to their fascinating properties such as high electronic conductivity, adjustable work function, high transparency, and good hydrophilicity.[29–31] In this work, we present a fully transparent UV photodetector based on TiO_2/MXene van der Waals heterojunction. By constructing a large number of local Schottky junctions at TiO_2/MXene interface, the responsivity can be dramatically improved by three orders of magnitude without affecting its spectral response characteristics. At the same time, derived from the high transparency of TiO_2 film and ultrathin MXene nanosheets, the designed device exhibits excellent transparency (95%). Unlike previous works that always use MXene as a Schottky contact electrode or carrier transport facilitator, here MXene was ingeniously selected to induce the photogating effect for the first time. We have systematically studied the photogating effect by ultraviolet photoelectron spectroscopy (UPS), Kelvin probe force microscope (KPFM), Finite element method (FEM) simulations, and density functional theory (DFT) calculations. Finally, a UV index (UVI) wireless sensing system that can be integrated into a smart window was demonstrated, exhibiting the promising application potential of this high-performance transparent TiO_2/MXene photodetector.

2. Results and Discussion

2.1. Device Structure and Material Characterizations

Figure 1a shows the schematic illustration of the designed TiO_2/MXene photodetector, in which MXene nanosheets are randomly distributed on the surface of the TiO_2 film, forming a large number of local Schottky junctions. And a pair of FTO electrodes with a spacing of 50 μm are preset at the bottom of the TiO_2 film. The specific fabrication process of the device is shown in Figure S1 (Supporting Information). Details about material preparation and device fabrication are described in the experimental section. Figure 1b shows the X-ray diffraction (XRD) patterns of the prepared TiO_2 film. Excluding the diffraction peaks of the FTO electrode, all the peaks are consistent with the anatase phase TiO_2, indicating the film has no impurity phase (such as rutile), which will contribute to the transport of carriers in the film. The Raman spectrum (Figure S2, Supporting Information) also confirms the good purity and crystallinity of the TiO_2 film.

Figure 1c presents the scanning electron microscopic (SEM) image of the TiO_2 film. It can be seen that the film has a dense and flat structure formed by fine crystal grains, which not only facilitates the good adhesion of MXene nanosheets on the film surface, but also blocks the conduction between the MXene and the FTO electrodes to avoid increasing dark current. The thickness of the TiO_2 film is ≈230 nm according to the cross-sectional SEM image (Figure S3, Supporting Information). The morphology of MXene nanosheets was observed by transmission electron microscope (TEM). As shown in Figure 1d, the prepared MXene exhibits an ultrathin sheet morphology with a lateral size close to 2 μm, indicating that $Ti_3C_2T_x$ was successfully delaminated via lithium ions intercalation and ultrasound. Inset shows the selected area electron diffraction of the MXene nanosheets with a typical hexagonal symmetric diffraction pattern, implying its good crystallinity. The changes in the XRD diffraction patterns and Raman spectra (Figure S4, Supporting Information) of MXene after etching and ultrasound are consistent with those reported results in the literature,[32–34] which further confirms the successful preparation of MXene nanosheets. The SEM image in Figure 1e shows the surface morphology of the fabricated device. It can be clearly observed that numerous MXene nanosheets are randomly attached to the surface of the TiO_2 film, indicating that the designed van der Waals heterojunction structure has been successfully realized.

2.2. Photodetection Performance and Transparency

Next, we comprehensively compared the photodetection performance of TiO_2/MXene and pure TiO_2 photodetectors. The responsivity (R) is the core parameter of the photodetector, which represents the photocurrent (defined as the current difference between light and dark state, $I_{ph} = I_{light} - I_{dark}$) excited by the per unit light power and can be calculated by the following formula:

$$R = I_{ph} / (P \cdot S) \tag{1}$$

where P is the light power density and S is the effective illumination area. **Figure 2**a shows the spectral responsivity of

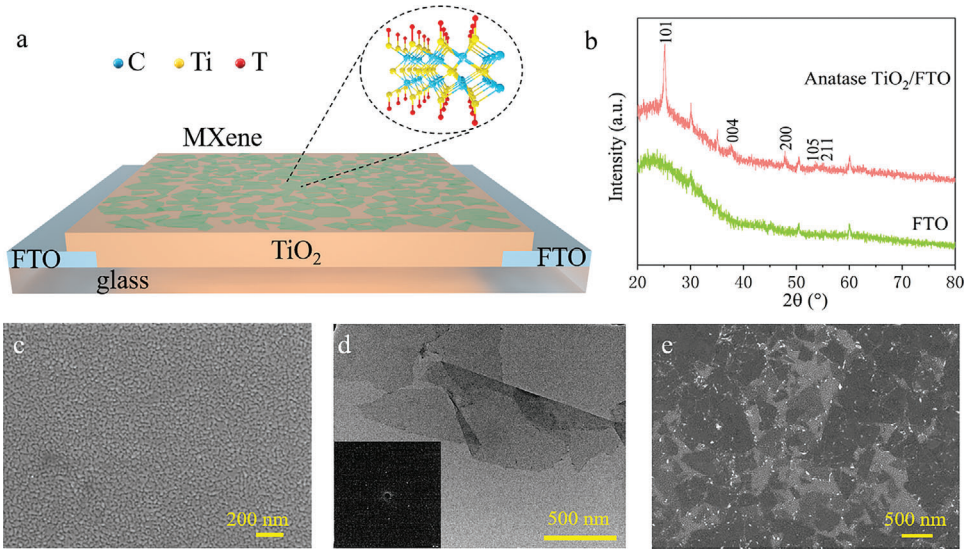

Figure 1. Device Structure and Material Characterizations. a) Schematic illustration of the TiO_2/MXene photodetector. b) XRD patterns of the FTO electrodes and prepared TiO_2 film. c) SEM image of the annealed TiO_2 film. d) TEM image of MXene nanosheets, inset is the SAED pattern. e) SEM image of the van der Waals heterojunctions at the surface of the device.

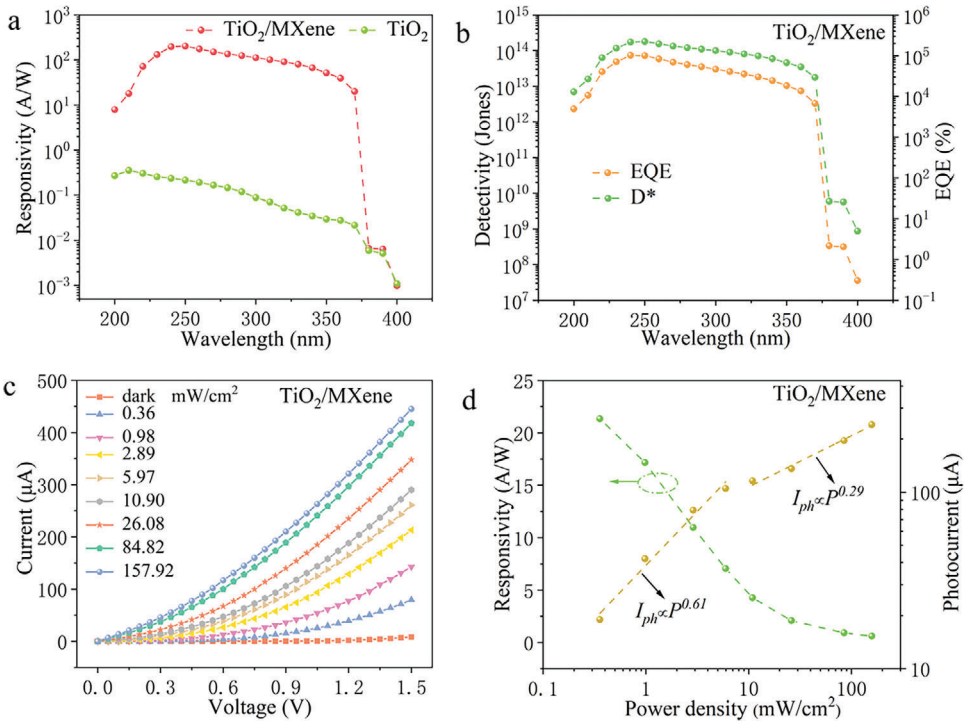

Figure 2. Wavelength- and light power-dependent photoresponse a) Spectral responsivity of the TiO_2/MXene and pure TiO_2 photodetectors at 1 V. b) Spectral D^* and EQE of the TiO_2/MXene photodetector. c) *I–V* curves of the TiO_2/MXene photodetector under different light power densities at 360 nm. d) Photocurrent and responsivity of the TiO_2/MXene photodetector under different light power densities.

TiO_2/MXene and pure TiO_2 photodetectors at 1 V. It can be seen that the responsivities of both devices are less than 0.01 A/W in the 380–400 nm wavelength range due to the large bandgap of TiO_2, but when the wavelength is reduced to 370 nm, the responsivity of the TiO_2/MXene photodetector sharply increases to 20 A/W, while that of the pure TiO_2 photodetector is only 0.02 A/W. Figure S5 (Supporting Information) plots the enhancement ratio ($R_{TiO2/MXene}/R_{TiO2}$) of responsivity at different wavelengths. The responsivity is improved by nearly three orders of magnitude in the wide UV wavelength range, and the highest enhancement

ratio is up to 1924 at 340 nm. The significant enhancement in responsivity is attributed to the fact that the built-in electric fields generated by the numerous local TiO_2/MXene Schottky junctions drive the efficient separation of photogenerated e-h pairs. The responsivity of the TiO_2/MXene photodetector reaches the peak of 202.4 A/W at 250 nm, making the device exhibit an ultrahigh UV/visible rejection ratio ($R_{250\ nm}/R_{400\ nm}$) of 2.05×10^5. The UV-visible absorption spectrum of the TiO_2 film shown in Figure S6 (Supporting Information) corresponds to this result. Notably, Figure S6, Supporting Information also shows that randomly distributed ultrathin MXene nanosheets have almost no interference on the absorption characteristics of the TiO_2 film. The external quantum efficiency (EQE) represents the ratio of collected carriers to incident photons, and the specific detectivity (D*) reflects the ability to detect weak light. These two important parameters can be calculated by Equations (2) and (3).

$$\mathrm{EQE} = (R \cdot h \cdot c) / (\lambda \cdot q) \tag{2}$$

$$D^* = R \cdot \sqrt{S / (2 \cdot q \cdot I_d)} \tag{3}$$

where h is the Plank constant, c is the velocity of light, λ is the wavelength, q is the elementary charge, and I_d is the dark current. As shown in Figure 2b, TiO_2/MXene photodetector exhibits a very high EQE of 1.02×10^5%, which indicates that more than 1000 carriers are collected under the excitation of a single photon. This result stems from the fact that holes with prolonged lifetimes trapped at the van der Waals interface break the charge neutrality in the channel and consequently induce more electrons from the source.[35] Since the photocurrent (signal) increases significantly while the dark current (noise) remains almost constant, the D* of the TiO_2/MXene photodetecotr is as high as 1.79×10^{14} Jones, suggesting its good ability to detect weak light. As a comparison, the performance of pure TiO_2 photodetector is much inferior, with peak EQE and D* being 210% and 5.57×10^{11} Jones respectively (Figure S7, Supporting Information).

In addition to wavelength, we have also investigated the light power-dependent photoreponse of the presented photodetector. Figure 2c plots the *I–V* curves of the TiO_2/MXene photodetector under different light power densities at 360 nm. As the light power density increases, the photocurrent under the same applied bias voltage also continuously increases. The photocurrent under different light power densities at 1 V is plotted in Figure 2d and their quantitative relationship can be fitted by a power law shown in Equation (4).

$$I_{ph} \propto P^{\alpha} \tag{4}$$

where α is the power exponent reflecting the linearity between photocurrent and light power density with an ideal value of 1. As shown in Figure 2d, two distinct linear regions can be observed as the light power density increases, implying different photoresponse processes under low and high-power illumination. Under low-power illumination, the photogeneration efficiency of charge carrier is proportional to the absorbed photon flux because the light absorption is not yet saturated. In addition, the photogating effect induced by MXene nanosheets effectively inhibits the recombination of photogenerated electrons and holes. As a result, the photocurrent increases with a higher power exponent (0.61). Under high-power illumination, the light absorption tends to be saturated and the trap states of hole is gradually filled, so the photocurrent increases slowly with light power density, that is, the power exponent (0.29) deviates far from 1.[36] The phenomenon that power exponent α deviates from 1 and varies with the light power range is consistent with other reported photodetectors dominated by the photogating effect.[26,37–39] As a counterevidence, the pure TiO_2 photodetector without photogating effect exhibits a good linearity with a power exponent of 0.83 in a wide range of light power density (Figure S8, Supporting Information). Figure 2d also plots the responsivity of the TiO_2/MXene photodetector as a function of light power density. The responsivity reaches the maximum value of 21.34 A/W at the minimum power density, which is still three orders of magnitude higher than the 14.83 mA W^{-1} of the pure TiO_2 photodetector (Figure S8, Supporting Information).

Good dynamic response characteristics are essential for the practical application, so the time-resolved photoresponses of the TiO_2/MXene and pure TiO_2 photodetectors have also been measured. As shown in **Figure 3**a, both devices exhibit stable photoswitching behaviors, but the photocurrent of the former 197 µA is much larger than that of the latter 0.62 µA. In contrast, the dark current only increased from 3 to 10 nA because the TiO_2 film isolates the conductive MXene nanosheets from the FTO electrodes. Compared with those cases where MXene is incorporated into the photosensitive layer to promote carrier separation and transport, this method achieves the largest increase in photocurrent and the smallest increase in dark current,[40–43] leading to an ultrahigh on/off ratio (I_{light}/I_{dark}) of 1.97×10^5 in the TiO_2/MXene photodetector. The shapes of the photo-switching curves show the obvious difference between the two photodetectors, implying their different carrier dynamics process. The photoresponse of the TiO_2/MXene photodetector shows a typical photoconductive relaxation process, that is, the photocurrent gradually increases with the illumination time. This is because the generation rate of photogenerated e-h pairs during continuous illumination is greater than the recombination rate due to the photogating effect. For the pure TiO_2 photodetector, the photocurrent increases rapidly and then gradually decays due to the subsequent high recombination rate. The response times can be obtained from the enlarged view of single cycle. As shown in Figure 3b, the pure TiO_2 photodetector shows a fast response speed with rise time and decay time of 0.19 and 0.23s, respectively. Since the trapping and de-trapping of holes in the direction perpendicular to the carrier transport involves more complex carrier dynamics processes, the response speed of the TiO_2/MXene photodetector is relatively slow with the rise time and decay time of 0.59 and 5.81 s, respectively. Compared with the substantial increase in photocurrent, a slight reduction in response speed is acceptable, especially for some applications that require high on/off ratio. High transparency is another fascinating feature of the TiO_2/MXene photodetector, so we measured the transmittance spectrum of the device. As shown in Figure 3c, the device exhibits a high transmittance of up to 95% in the visible and near-infrared regions (the slight absorption at 600 nm should be caused by the optical interference of the TiO_2 film). The photograph in the inset further confirms the high transparency of the device. The effects of the

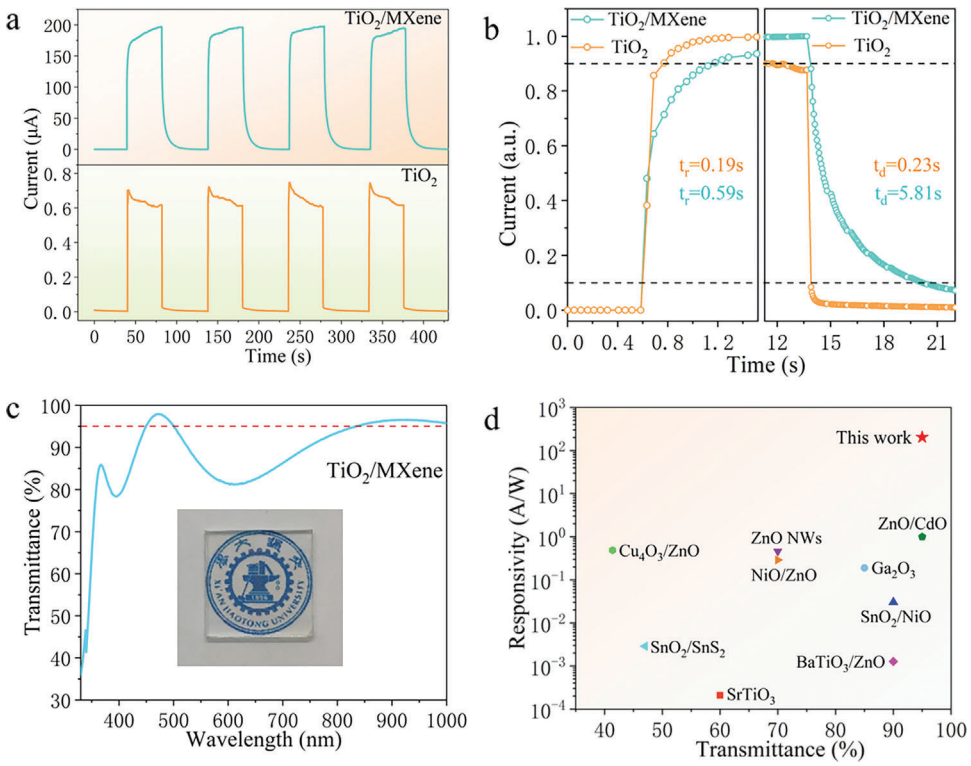

Figure 3. Dynamic response characteristics and transparency a) Time-resolved photoresponse measurements of the TiO_2/MXene and pure TiO_2 photodetectors at 360 nm. b) Rise (t_r) and decay (t_d) times the TiO_2/MXene and pure TiO_2 photodetectors. c) Transmittance spectrum of the TiO_2/MXene photodetector, inset is a photograph of the fully transparent device. d) The performance comparison of TiO_2/MXene photodetector with other reported transparent photodetectors.

thickness of TiO_2 film and MXene layer on the device performance and transparency have been taken into account, as discussed in detail in Figure S9–S11 (Supporting Information). In order to intuitively reflect the performance level of our device, the two key parameters of transparent photodetectors, responsivity, and transparency, are compared with previously reported transparent metal oxide-based UV photodetectors.[17,44–51] As shown in Figure 3d, the TiO_2/MXene photodetector exhibited simultaneously the highest responsivity and transparency among the compared devices. Such superior performance is a result of ingenious material selection and device structure design. The low absorption of TiO_2 film in the visible region as well as the atomic thickness of MXene nanosheets ensure the high transmittance of the device. Meanwhile, the photogating effect induced by TiO_2/MXene van der Waals heterojunctions endows it an ultrahigh responsivity. Stability is one of the key issues for MXene-based optoelectronic devices, so the stability of TiO_2/MXene photodetector has also been investigated, see Figure S12 (Supporting Information) for details.

2.3. Investigation of the Working Mechanism

In order to experimentally confirm that the photogating effect is the dominant mechanism for the photoconductive gain of the TiO_2/MXene photodetector, UPS and KPFM tests were performed. From the UPS shown in **Figure 4**a, the work functions of the MXene and TiO_2 films are determined to be 4.54 and 4.21 eV, respectively. Accordingly, local Schottky junctions are formed between the TiO_2 film and the MXene nanosheets randomly distributed on the surface. Figure 4b illustrates the band structure and carrier distribution of the Schottky junction under illumination. Electrons tunnel from TiO_2 to MXene due to its lower Fermi level, leaving an equal number of holes in the TiO_2 film. When reaching equilibrium, their Fermi levels tend to be the same and a depletion zone is formed in the TiO_2 film near the interface. In the depletion zone, the conduction band (E_C) of TiO_2 bends upward toward MXene and there is a built-in electric field directed from TiO_2 to MXene. Under UV illumination, a large number of e-h pairs are generated in the TiO_2 film, and then the holes migrate to the surface of the TiO_2 film driven by the built-in electric fields and are finally trapped at the TiO_2/MXene interface. Meanwhile, electrons are collected by FTO electrodes at the bottom of the TiO_2 film driven by an external electric field. In the above process, the trapped holes have a prolonged lifetime due to the difficulty in recombining with electrons. The lifetime is longer than the transit time of the electron in the channel, so when the photogenerated electron reaches the anode, another electron will immediately enter the channel from the cathode to maintain charge neutrality. This process repeats until the excess electrons recombine with holes.[21] The electron generated under the excitation of a single photon circulates multiple times in the circuit before recombination, which is the reason why our device exhibits an ultrahigh EQE. The quenched fluorescence intensity of the TiO_2

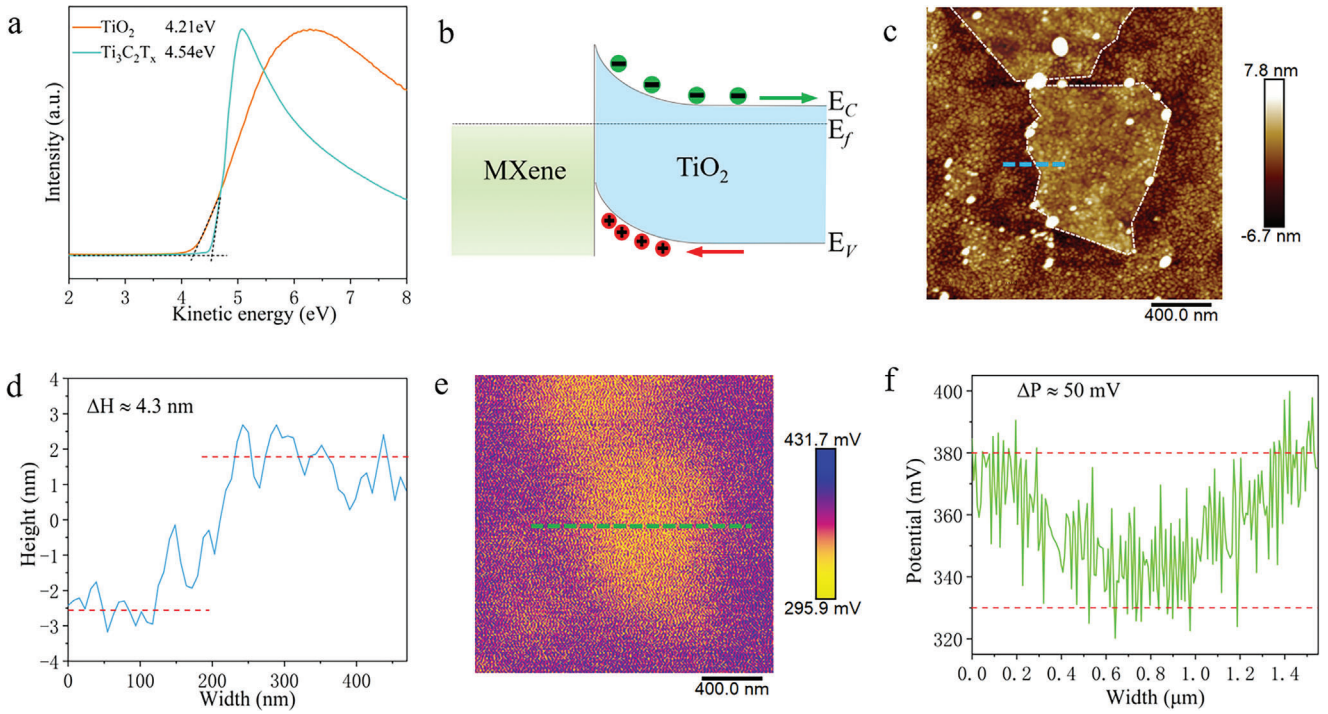

Figure 4. Experimental investigations on the working mechanism. a) UPS spectra of the MXene nanosheets and TiO_2 film. b) Band structure diagram of the TiO_2/MXene heterojunction based on UPS spectra. c) The AFM image of the TiO_2/MXene heterojunction. d) Height profile of the MXene nanosheet measured along the blue line in (c). e) KPFM image corresponding to (c). f Surface potential along the green line in (e).

film after forming heterojunctions with MXene also confirmed that the carrier recombination was significantly inhibited (Figure S13, Supporting Information). To further verify the formation of the local Schottky junctions in the mesoscopic scale, the KPFM measurement was carried out. Figure 4c shows the atomic force microscope (AFM) morphology of MXene nanosheets on the surface of TiO_2 film. The height profile measured along the blue dashed line in Figure 4c shows that the thickness of the MXene nanosheet is about 4.3 nm (Figure 4d), which corresponds to the thickness of 3 layers according to the previous literature.[52] The KPFM image in Figure 4e shows the surface potential mapping corresponding to Figure 4c. It can be clearly seen that the area covered by MXene has a lower electric potential than the bare TiO_2 film, which proves that there is a built-in electric field directed from the TiO_2 film to the MXene nanosheet.[53] Figure 4f shows the surface potential profile along the green dashed line in Figure 4e, from which there is a potential drop of about 50 mV from the TiO_2 film to the MXene nanosheet.

To gain further insight into the working mechanism of the TiO_2/MXene photodetector, FEM simulations (COMSOL Multiphysics) was performed to clarify spatial distributions of electrons and the built-in electric field. In the 2D model of **Figure 5**, the thickness of the TiO_2 film was set to 230 nm according to the SEM measurement, while the work function of the MXene nanosheets located at the upper side of the TiO_2 film was set to be 4.54 eV according to the UPS measurement. Figure 5a shows the spatial distribution of electrons. It can be seen that the electron concentration near the Schottky interface is far lower than that in the bulk of TiO_2 film, which is due to the transfer of electrons in the depletion region to the MXene nanosheets. The result in Figure 5b shows that the built-in electric field reaches a maximum value at the interface between TiO_2 film and MXene nanosheets, and gradually decreases towards the bulk of TiO_2 film. As pointed by the white arrows, the direction of the built-in electric field is from TiO_2 to MXene, which is consistent with the above experimental results. DFT calculations were performed to further reveal the charge transfer and potential distribution at the TiO_2/MXene interface. Since the surface termination (such as F, OH, and O) significantly affects electrical properties (especially the work function) of MXene, the composition of surface terminations was extracted by X-ray photoelectron spectroscopy (XPS) measurements before DFT calculations. XPS test results (Figure S14, Supporting Information) indicate that the surface terminations contain approximately 67% F, 26% OH, and 7% O, which are consistent with the fact that a high concentration of LiF was used during the etching process. Therefore, the composition of MXene is reasonably simplified as $Ti_3C_2F_2$ in the computational model. Figure 5c shows the charge density difference of the TiO_2/MXene heterojunction, where the cyan and yellow regions represent the loss and gain of electrons, respectively. It can be clearly seen that MXene gains electrons while TiO_2 loses electrons when they contact with each other. Further, the electrostatic potential of TiO_2/MXene heterojunction was calculated and depicted in Figure 5d. There is a vacuum electrostatic potential difference of 1.8 eV between TiO_2 and MXene, which indicates that the work function of MXene is larger than that of TiO_2. Note that there is a difference from the KPFM test result (Figure 4f), because the theoretical calculation results are only affected by the intrinsic physical properties of the materials, but the KPFM test is also affected by measurement errors

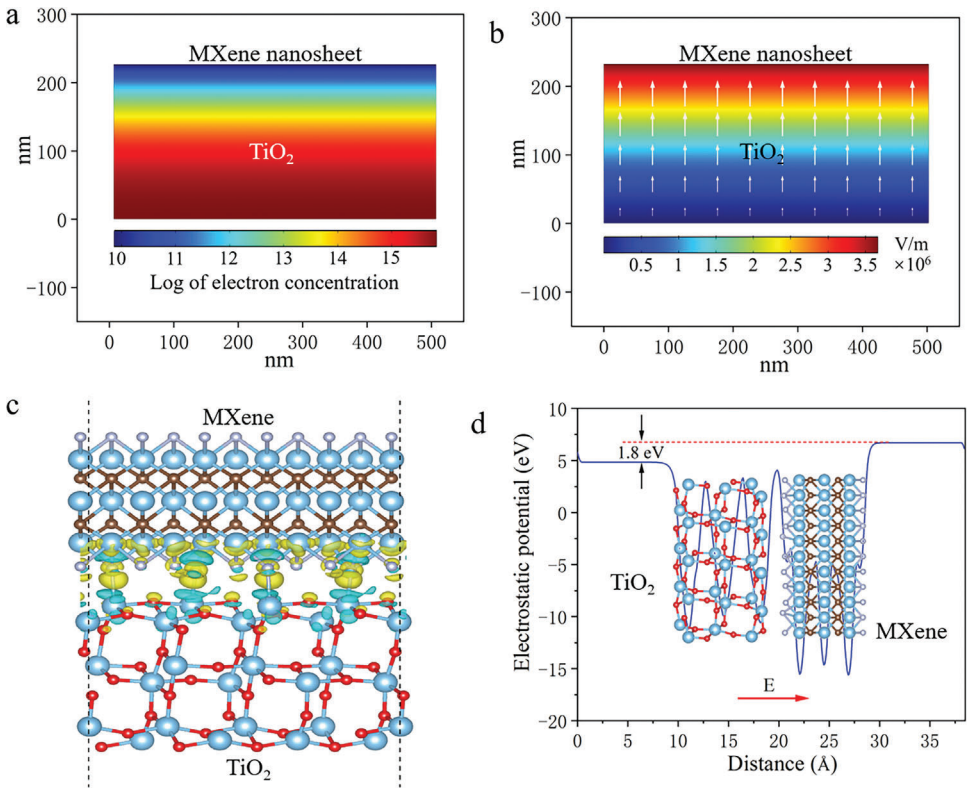

Figure 5. Simulations and theoretical calculations on the working mechanism. Distributions of a) electrons and b) the built-in electric field simulated at the TiO_2/MXene interface. c) Charge density difference of the $TiO_2/Ti_3C_2F_2$ heterojunction (a scale unit of 2×10^{-3} e/Å^3). The big light blue, red, brown, and small light gray balls represent Ti, O, C, and F atoms, respectively. The cyan and yellow areas indicate electron loss and gain, respectively. d) Calculated electrostatic potential of TiO_2/ $Ti_3C_2F_2$ heterojunction.

and impurity adsorption. The order of the potential levels obtained by the two methods is consistent, which is what really matters. In addition, the average potential at the MXene side is lower than that of the TiO_2 side, suggesting the existence of an interfacial coupled built-in electric field from TiO_2 to MXene, as pointed by the red arrow. All the results of theoretical calculations, experiments, and simulations are consistent well, strongly confirming the transfer of charges and the establishment of the built-in electric field at the TiO_2/MXene interface. Hence, the photogating effect induced by this van der Waals heterojunction is believed to be the origin of the excellent photoconductive gain.

2.4. Device Application

The monitoring of UVI is one of the common applications of UV photodetectors. However, some special applications requiring transparent electronics, such as smart windows, are difficult to realize with opaque commercial UV intensity meters. In view of the high transparency, responsivity, and UV/visible rejection ratio of the presented TiO_2/MXene photodetector, a proof-of-concept UVI wireless sensing smart system is demonstrated. **Figure 6**a depicts a conceived application scene, in which a fully transparent TiO_2/MXene photodetector is integrated on the window. The information of detected UV intensity will be transmitted to a smartphone via Bluetooth and converted into an UVI for real-time display. In this way, we can easily check the UVI in real time before going out and take corresponding protective measures to avoid UV sunburn. Figure 6b shows the photocurrent recorded by the TiO_2/MXene photodetector attached to a south-facing window from morning to afternoon. The device exhibits an obvious photoresponse under sunlight illumination and the change of photocurrent in line with the variation trend of UV intensity within a day, indicating its feasibility for real-time UV monitoring. Note that the possibility that the photocurrent fluctuation is caused by temperature changes has been excluded (see Figure S15, Supporting Information). Figure 6c illustrates the definition and exposure category of the UVI. The UVI is a measure of the intensity of UV radiation on the Earth's surface that is relevant to effects on human skin, and it is defined by the calculus formula shown in Figure 6c, where E_λ is the solar spectral irradiance (W m^{-2} nm^{-1}), S_{er} is the erythema reference action spectrum, and K_{er} is a constant (40 m^2 W^{-1}).[54] UVI values are grouped into five exposure categories based on size ranges, representing different UV levels and exposure risks. Figure 6d shows a photograph of a real-life application scene, in which the UVI detected by the transparent TiO_2/MXene photodetector exposed to sunlight was displayed on the smartphone. The dynamic results under sunlight and artificial UV light can also be found in Supporting Information, Movies S1 and S2, Supporting Information.

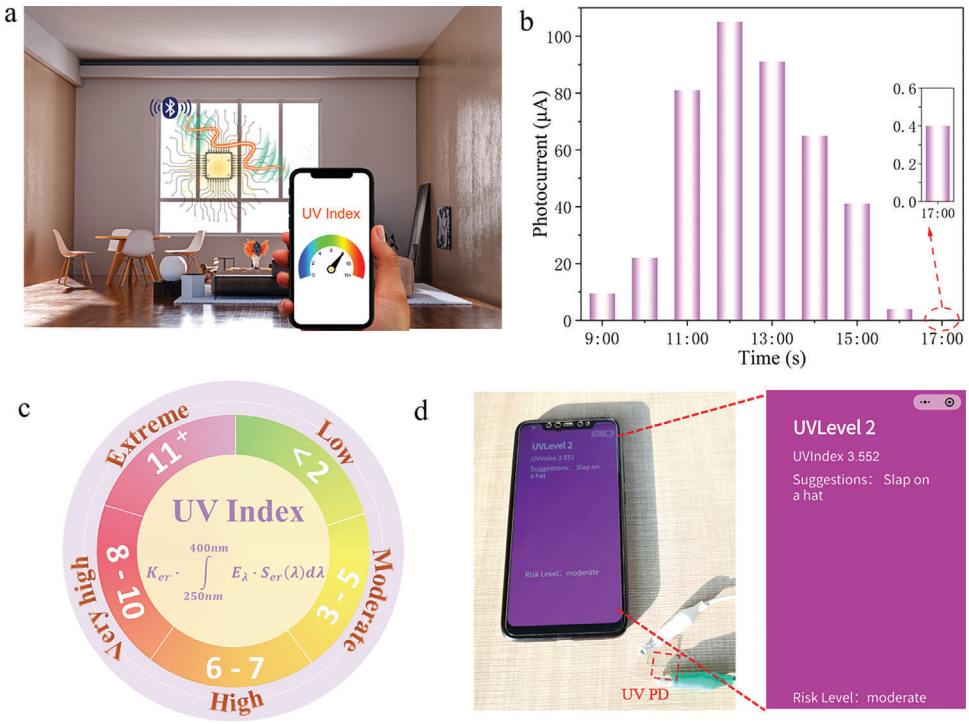

Figure 6. Device application: UVI wireless sensing system. a) Schematic diagram of the transparent TiO_2/MXene photodetector integrated in a smart window for real-time UVI monitoring. b) Photocurrent measured by the transparent TiO_2/MXene photodetector on a south-facing window under sunlight from 9:00-17:00. c) Definition and exposure category of the UVI. d) A photograph of monitoring the UVI in real time under sunlight and enlarged monitoring result on the smartphone.

3. Conclusions

In summary, we have successfully demonstrated an all-solution-processed UV photodetector with high transparency up to 95%. The fully transparent photodetector has a simplified structure based on TiO_2/MXene van der Waals heterojunction. The device possesses outstanding performance including ultrahigh responsivity (202.4 A W^{-1}), large detectivity (1.79×10^{14} Jones) as well as extremely high on/off ratio (2×10^5) at a small bias of 1 V. Experimental tests (UPS and KPFM), FEM simulations, and DFT calculations were carried out to deeply reveal the working mechanism. The giant photogating effect induced at the TiO_2/MXene interface can significantly suppress the recombination of photogenerated carriers, leading to the improved photoelectric conversion behavior and enhanced photodetection performance. Based on the advantages of this transparent photodetector, a UVI wireless sensing system expected to be integrated into smart windows is demonstrated as a proof-of-concept. This work sheds light on the design of high-performance transparent photodetectors and demonstrates the promising application of MXene in optoelectronics.

4. Experimental Section

Materials Synthesis: The TiO_2 film was prepared by a sol-gel method. To synthesize the precursor, 9 ml of ethylene glycol methyl ether (AR, Sinopharm Chemical Reagent Co., Ltd.) and 3 ml of tetrabutyl titanate (98%, Sinopharm Chemical Reagent Co., Ltd.) were mixed and stirred. Then 2 ml of acetic anhydride (AR, Sinopharm Chemical Reagent Co., Ltd.) was added dropwise as a stabilizer. The resulting mixture was continuously stirred for 3 h and allowed to stand for 24 h for aging to obtain a transparent yellow precursor.

$Ti_3C_2T_x$ MXene nanosheets are synthesized by selective etching of the Al layer from the MAX phase Ti_3AlC_2 (Jilin 11 Technology Co., Ltd.). Specifically, 1.6 g LiF (98%, Sinopharm Chemical Reagent Co., Ltd.) was slowly added to 20 ml concentrated HCl (12 M, Sinopharm Chemical Reagent Co., Ltd.) in a Teflon beaker and stirred for 10 min to dissolve. 1 g MAX phase powder is slowly added to the above-mixed solution and continuously stirred for 24 h in an oil bath at 40 °C to etch away the Al layer. Subsequently, the resulting mixture was washed several times with deionized water by centrifugation (3500 rpm for 5 min) until the PH of the supernatant was about 6. After that, deionized water was added to the washed sediment and the mixture was ultrasonicated in an ice bath for 1 h to delaminate the multilayer MXene. Finally, the resultant after ultrasound was centrifuged at 3500 rpm for 1 h, and the resulting supernatant, a dark green colloid solution containing few or single layers of MXene nanosheets was collected.

Device Fabrication: The glass substrate with FTO electrodes (50 μm channel) is ultrasonically cleaned with acetone, ethanol, and deionized water in sequence. The prepared TiO_2 precursor was spin-coated on the glass substrate at 4000 rpm for 20 s. Then the resulting film was immediately baked on a 350 °C hot plate for 30 min to remove residual organics. The spin coating and baking process were repeated three times to obtain a desired thickness. After that, the film was annealed at 500 °C in air for 2 h to crystallize. Finally, the MXene colloidal solution was spin-coated on the surface of the annealed TiO_2 film at 3000 rpm for 20 s, and the resulting device was baked in a N_2 glove box at 120°C for 10 min to promote the contact between the MXene nanosheets and the TiO_2 film. Notably, lead parts of the FTO electrodes were attached with high-temperature resistant tape during the spin-coating of TiO_2 precursor and MXene colloidal solution to reduce contact resistance and prevent short circuit during testing, as shown in Figure S1 (Supporting Information).

Characterization: The crystal structure and phase identification of TiO_2 film and MXene were performed by XRD (Bruker D8 ADVANCE) with Cu Kα radiation. Raman spectra were collected by a Raman spectroscopy (LabRAM HR Evolution) equipped with a 532 nm laser. The morphologies of the samples were observed by SEM (Zeiss Gemini500) and TEM (JEOL JEM-F200). The chemical compositions and work functions of the samples were tested through XPS (Thermo Fisher ESCALAB Xi+). The steady-state photoluminescence (PL) spectra were tested through a transient steady-state fluorescence spectrometer (Edinburgh FLS9) with a 325 nm laser. The thickness test of MXene nanosheet and KPFM measurement were carried out through AFM (Bruker Dimension Icon). The photoelectric performance tests of the device were carried out through a digital sourcemeter (Keithley 2410), a 360 nm laser (CNI, UV-F-360-80 mW) with adjustable light power and a monochromatic light source (Zolix, Omni-λbright) with adjustable wavelength. The light power was calibrated by an optical power meter (OPHIR photonics, Israel).

Density Functional Theory Calculation: All calculations for $TiO_2/Ti_3C_2F_2$ heterostructure were performed based on the DFT with the projector-augmented-wave pseudopotentials implemented in the Vienna ab initio simulation package.[55,56] A kinetic energy cutoff in the plane-wave expansion was set as 450 eV. The 2D Brillouin zone was sampled with $8 \times 2 \times 1$ Monkhorst–Pack k-points grids.

Supporting Information

Supporting Information is available from the Wiley Online Library or from the author.

Acknowledgements

This work was supported by the National Natural Science Foundation of China (No. 51902250). H.W. acknowledged the support of Shenzhen Science and Technology Program (No. KQTD20180411143514543). J.H. acknowledged the support of Beijing Natural Science Foundation, China (Grant No. Z190011). Theoretical calculations were performed using resources of the Supercomputer Centre in Chongqing. Instrument Analysis Center of Xi'an Jiaotong University and the shiyanjia lab (www.shiyanjia.com) was acknowledged for the great help in measurements.

Conflict of Interest

The authors declare no conflict of interest.

Data Availability Statement

The data that support the findings of this study are available from the corresponding author upon reasonable request.

Keywords

MXene nanosheets, photogating effect, transparent electronics, ultraviolet photodetectors, van der Waals heterojunction

Received: February 15, 2023
Published online: April 7, 2023

[1] F. P. García de Arquer, A. Armin, P. Meredith, E. H. Sargent, *Nat. Rev. Mater.* **2017**, *2*, 16100.
[2] J. Liu, F. Xia, D. Xiao, F. J. Garcia de Abajo, D. Sun, *Nat. Mater.* **2020**, *19*, 830.
[3] F. Teng, K. Hu, W. Ouyang, X. Fang, *Adv. Mater.* **2018**, *30*, 1706262.
[4] Y. Wang, Y. Liu, S. Cao, J. Wang, *J. Mater. Chem. C* **2021**, *9*, 5302.
[5] H. Khandelwal, A. P. H. J. Schenning, M. G. Debije, *Adv. Energy Mater.* **2017**, *7*, 1602209.
[6] H. Fang, H. Ma, C. Zheng, S. Lennon, W. Wu, L. Wu, H. Wang, *Appl. Surf. Sci.* **2020**, *529*, 147122.
[7] C. J. Traverse1, R. Pandey, M. C. Barr, R. R. Lunt, *Nat. Energy* **2017**, *2*, 849.
[8] J. F. Wager, *Science* **2003**, *300*, 1245.
[9] H. Fang, C. Zheng, L. Wu, Y. Li, J. Cai, M. Hu, X. Fang, R. Ma, Q. Wang, H. Wang, *Adv. Funct. Mater.* **2019**, *29*, 1809013.
[10] D. Zhang, Z. Xu, Z. Huang, A. R. Gutierrez, C. J. Blocker, C. H. Liu, M. B. Lien, G. Cheng, Z. Liu, I. Y. Chun, J. A. Fessler, Z. Zhong, T. B. Norris, *Nat. Commun.* **2021**, *12*, 2413.
[11] Q. Li, J. van de Groep, Y. Wang, P. G. Kik, M. L. Brongersma, *Nat. Commun.* **2019**, *10*, 4982.
[12] C. Xie, F. Yan, *Small* **2017**, *13*, 1701822.
[13] L. Shi, K. Chen, A. Zhai, G. Li, M. Fan, Y. Hao, F. Zhu, H. Zhang, Y. Cui, *Laser Photonics Rev.* **2021**, *15*, 2000401.
[14] M. Buscema, D. J. Groenendijk, S. I. Blanter, G. A. Steele, H. S. van der Zant, A. Castellanos-Gomez, *Nano Lett.* **2014**, *14*, 3347.
[15] L. Qian, Y. Sun, M. Wu, D. Xie, L. Ding, G. Shi, *Adv. Mater.* **2017**, *29*, 1606175.
[16] J. Park, Y. Park, G. Yoo, J. Heo, *Nanoscale Res. Lett.* **2017**, *12*, 599.
[17] Y. Zhang, X. Zhao, J. Chen, S. Li, W. Yang, X. Fang, *Adv. Funct. Mater.* **2019**, *30*, 1907650.
[18] X. Wang, P. Wang, J. Wang, W. Hu, X. Zhou, N. Guo, H. Huang, S. Sun, H. Shen, T. Lin, M. Tang, L. Liao, A. Jiang, J. Sun, X. Meng, X. Chen, W. Lu, J. Chu, *Adv. Mater.* **2015**, *27*, 6575.
[19] D. Zheng, H. Fang, P. Wang, W. Luo, F. Gong, J. C. Ho, X. Chen, W. Lu, L. Liao, J. Wang, W. Hu, *Adv. Funct. Mater.* **2016**, *26*, 7690.
[20] V. Adinolfi, E. H. Sargent, *Nature* **2017**, *542*, 324.
[21] H. Fang, W. Hu, *Adv. Sci.* **2017**, *4*, 1700323.
[22] T. Lei, H. Tu, W. Lv, H. Ma, J. Wang, R. Hu, Q. Wang, L. Zhang, B. Fang, Z. Liu, W. Shi, Z. Zeng, *ACS Appl. Mater. Interfaces* **2021**, *13*, 50213.
[23] N. Krishnan K, A. Sreedharan, S. Sagar, L. Thomas Manamel, A. Mukherjee, B. C. Das, *Appl. Surf. Sci.* **2021**, *568*,150818.
[24] T. H. Tsai, Z. Y. Liang, Y. C. Lin, C. C. Wang, K. I. Lin, K. Suenaga, P. W. Chiu, *ACS Nano* **2020**, *14*, 4559.
[25] H. Ma, Y. Xing, J. Han, B. Cui, T. Lei, H. Tu, B. Guan, Z. Zeng, B. Zhang, W. Lv, *Adv. Opt. Mater.* **2021**, *10*, 2101772.
[26] Z. Qi, T. Yang, D. Li, H. Li, X. Wang, X. Zhang, F. Li, W. Zheng, P. Fan, X. Zhuang, A. Pan, *Mater. Horiz.* **2019**, *6*, 1474.
[27] L. Ye, P. Wang, W. Luo, F. Gong, L. Liao, T. Liu, L. Tong, J. Zang, J. Xu, W. Hu, *Nano Energy* **2017**, *37*, 53.
[28] Z. Cai, M. Cao, Z. Jin, K. Yi, X. Chen, D. Wei, *npj 2D Mater. Appl.* **2018**, *2*, 21.
[29] H. Ma, L. Jia, Y. Lin, H. Fang, W. Wu, L. Wu, B. Hu, H. Wang, *Nanotechnology* **2021**, *33*, 075502.
[30] A. VahidMohammadi, J. Rosen, Y. Gogotsi, *Science* **2021**, *372*, 1165.
[31] K. Hantanasirisakul, Y. Gogotsi, *Adv. Mater.* **2018**, *30*, 1804779.
[32] M. Naguib, M. Kurtoglu, V. Presser, J. Lu, J. Niu, M. Heon, L. Hultman, Y. Gogotsi, M. W. Barsoum, *Adv. Mater.* **2011**, *23*, 4248.
[33] B. Li, Q. B. Zhu, C. Cui, C. Liu, Z. H. Wang, S. Feng, Y. Sun, H. L. Zhu, X. Su, Y. M. Zhao, H. W. Zhang, J. Yao, S. Qiu, Q. W. Li, X. M. Wang, X. H. Wang, H. M. Cheng, D. M. Sun, *Adv. Mater.* **2022**, *34*, 2201298.
[34] A. Ren, J. Zou, H. Lai, Y. Huang, L. Yuan, H. Xu, K. Shen, H. Wang, S. Wei, Y. Wang, X. Hao, J. Zhang, D. Zhao, J. Wu, Z. Wang, *Mater. Horiz.* **2020**, *7*, 1901.
[35] S. Lee, J. Park, Y. Yun, J. Lee, J. Heo, *Adv. Mater. Interfaces* **2019**, *6*, 1900053.

[36] C. Soci, A. Zhang, B. Xiang, S. A. Dayeh, D. P. R. Aplin, J. Park, X. Y. Bao, Y. H. Lo, D. Wang, *Nano Lett.* **2007**, *7*, 1003.
[37] Q. Liang, Q. Wang, Q. Zhang, J. Wei, S. X. Lim, R. Zhu, J. Hu, W. Wei, C. Lee, C. Sow, W. Zhang, A. T. S. Wee, *Adv. Mater.* **2019**, *31*, 1807609.
[38] C. Yin, C. Gong, J. Chu, X. Wang, C. Yan, S. Qian, Y. Wang, G. Rao, H. Wang, Y. Liu, X. Wang, J. Wang, W. Hu, C. Li, J. Xiong, *Adv. Mater.* **2020**, *32*, 2002237.
[39] C. Hu, D. Dong, X. Yang, K. Qiao, D. Yang, H. Deng, S. Yuan, J. Khan, Y. Lan, H. Song, J. Tang, *Adv. Funct. Mater.* **2017**, *27*, 1603605.
[40] H. Li, Z. Li, S. Liu, M. Li, X. Wen, J. Lee, S. Lin, M. Y. Li, H. Lu, *J. Alloys Compd.* **2022**, *895*, 162570.
[41] M. Y. Li, Z. Li, H. Li, S. Liu, H. Lu, X. Wen, Y. Yang, *ACS Appl. Nano Mater.* **2021**, *4*, 13674.
[42] W. Ouyang, J. Chen, J. H. He, X. Fang, *Adv. Electron. Mater.* **2020**, *6*, 2000168.
[43] V. Selamneni, V. Adepu, H. Raghavan, P. Sahatiya, *FlatChem* **2022**, *33*, 100363.
[44] S. Abbas, D. K. Ban, J. Kim, *Sens. Actuators, A* **2019**, *293*, 215.
[45] S. Abbas, M. Kumar, D. W. Kim, J. Kim, *Small* **2019**, *15*, 1804346.
[46] A. Afal, S. Coskun, H. E. Unalan, *Appl. Phys. Lett.* **2013**, *102*, 043503.
[47] S. Cui, Z. Mei, Y. Zhang, H. Liang, X. Du, *Adv. Opt. Mater.* **2017**, *5*, 1700454.
[48] Z. Long, X. Xu, W. Yang, M. Hu, D. V. Shtansky, D. Golberg, X. Fang, *Adv. Electron. Mater.* **2020**, *6*, 1901048.
[49] A. K. Rana, M. Kumar, D. K. Ban, C. P. Wong, J. Yi, J. Kim, *Adv. Electron. Mater.* **2019**, *5*, 1900438.
[50] W. Yang, Y. Zhang, Y. Zhang, W. Deng, X. Fang, *Adv. Funct. Mater.* **2019**, *29*, 1905923.
[51] Z. Zheng, L. Gan, H. Li, Y. Ma, Y. Bando, D. Golberg, T. Zhai, *Adv. Funct. Mater.* **2015**, *25*, 5885.
[52] A. Lipatov, M. Alhabeb, M. R. Lukatskaya, A. Boson, Y. Gogotsi, A. Sinitskii, *Adv. Electron. Mater.* **2016**, *2*, 1600255.
[53] P. Cui, D. Wei, J. Ji, H. Huang, E. Jia, S. Dou, T. Wang, W. Wang, M. Li, *Nat. Energy* **2019**, *4*, 150.
[54] World Health Organization, World Meteorological Organization, United Nations Environment Programme & International Commission on Non-Ionizing Radiation Protection. Global solar UV index: a practical guide, **2002**, https://extranet.who.int/iris/restricted/handle/10665/42459.
[55] G. Kresse, J. Furthmüller, *Phys. Rev. B* **1996**, *54*, 11169.
[56] G. Kresse, J. Furthmüller, *Comput. Mater. Sci.* **1996**, *6*, 15.

